ASME Journal of Turbomachinery
Online journal at:
https://asmedigitalcollection.asme.org/turbomachinery

Compressor Tip Leakage Mechanisms

James V. Taylor[1]
Whittle Laboratory,
University of Cambridge,
Cambridge CB3 0DY, UK
e-mail: jvt24@cam.ac.uk

Anthony M. J. Dickens
Whittle Laboratory,
University of Cambridge,
Cambridge CB3 0DY, UK

Harry Simpson
Rolls-Royce plc,
Derby DE24 9HY, UK

The over tip leakage flow in an unshrouded compressor blade row is highly three dimensional, yet in order for aerodynamicists to analyze and improve designs, they must be able to simplify the problem down to a limited number of mechanisms. In this article, the behaviors of the dominant loss mechanisms are investigated using a multi-order methodology that combines rapid experimental tests of different geometries, detailed measurements in a large rotating rig, large numbers of industry-standard 3D Reynolds-averaged Navier–Stokes (RANS) simulations, and a single direct numerical simulation (DNS) of the datum geometry. The three loss mechanisms identified are ultimately caused by mismatches in flow velocity: separation of the flow as it enters the gap, mixing of the leakage jet with the mainstream close to the suction surface, and endwall shear acting on the jet itself at mid passage. This article is presented in three sections: First, the loss mechanisms are visualized and examined in detail using experiment, simulation, and models. Second, the uncertainty in industry-standard predictions is analyzed and improvements to turbulence modeling are presented. Finally, a matrix of blades with different 3D designs is used to investigate the balance of loss mechanisms and a reduction in total loss generation.

[DOI: 10.1115/1.4064317]

Keywords: cavity and leaking flows, computational fluid dynamics (CFD), fan, compressor, and turbine aerodynamic design, measurement techniques, turbomachinery blading design

1 Introduction

Tip leakage losses in axial compressors are significant and account for up to a third of the total loss [1]. Losses occur as the blade pressure difference drives the flow over the casing-end tip gap of all rotors and the hub-end tip gap of unshrouded stator blades. Figure 1 shows the dissipation coefficient, a nondimensional measure of the viscous dissipation, calculated from an instantaneous time snapshot of a DNS solution of an unshrouded stator blade. A single threshold of 0.25 is applied to show that the total loss is created from three distinct mechanisms.

Blue shows the loss generated within the tip gap itself; as the flow accelerates into the gap, it separates from the sharp pressure side corner, and this subsequently mixes out and reattaches before reaching the suction side of the gap. Red shows the loss in the plane of the blade tip caused by mixing of the jet with the mainstream flow; the pressure difference across the gap causes the leakage flow to exit at an angle significantly different to the suction side velocity. Yellow shows loss at 10% of gap height caused by shear on the endwall surface; the largest velocity discrepancies between the spinning endwall and the local flow occur at mid-pitch after the leakage jet has undergone mixing, and its tangential velocity is reduced.

Early work in the field has concentrated on the mainstream mixing mechanism, with papers, low-order design codes, and even undergraduate courses and exams on calculating this loss [2,3,1,4]. Many following works focus on the possible presence of a tip leakage vortex and its motion within the passage [5–7]. However, this is disputed in the work of Maynard et al. [8] who showed that the unsteadiness of smaller scale turbulent structures dominate the flowfield and that the tip leakage vortex is only visible in the time average flow. Early Navier–Stokes solvers [9] even showed that the region with the most significant loss generation occurs adjacent to the suction surface, in the shear layer formed between leakage jet and mainstream, before the flow could possibly roll up into a vortex.

The within-gap mixing loss is mentioned in the literature but is often neglected. Historically, this was to enable low-order modeling or pinched tip calculations like those in Ref. [4]. Note that their assumption of zero within-gap loss was conditional on the flow remaining detached across the entirety of the blade tip after it separated from the sharp pressure side edge. Maynard et al. in Ref. [8] have since shown that the flow reattaches even in large clearances of 3.2% chord, and this means that the assumption of zero within-gap loss does not apply in most practical cases. In their work, they also examined the unsteady structure of the flow within the gap, the mechanisms for loss generation, and the effect of locally rounded blade tips.

Losses on the endwall surface have not been given the same attention. Many cascade experiments and models do not include the relative motion of the wall, and so it is natural to neglect this mechanism. Recently, Ventosa-Molina et al. [10] showed that relative endwall motion has a significant effect on the structure of the flow, and so it must be considered for accurate results. All modern CFD calculations or experiments in rotating machines

---

[1] Corresponding author.

Contributed by the International Gas Turbine Institute (IGTI) of ASME for publication in the Journal of Turbomachinery. Manuscript received September 21, 2023; final manuscript received November 30, 2023; published online January 16, 2024. Assoc. Editor: David G. Bogard.

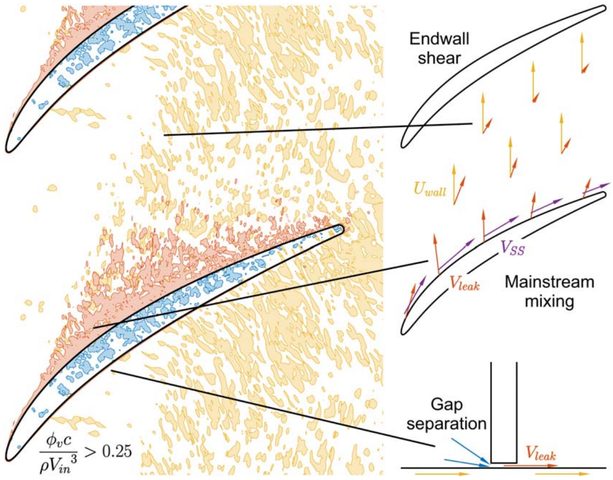

Fig. 1 Three loss mechanisms in competition confound predictions, design, and understanding. Regions of significant dissipation extracted from instantaneous DNS calculation, velocity vectors from time average.

will include the endwall loss mechanism, but it is never isolated for study or comparison.

This article shows that the within-gap and endwall loss mechanisms are just as important as the jet mixing with the mainstream. It also shows that the accuracy of prediction differs for each loss mechanism. This hinders attempts to design compressors with reduced tip leakage losses; predictions do not often match experiments, and neglecting one or more of the loss mechanisms will confound interpretations of the results.

The first section of this article examines and visualizes each of the three tip leakage loss mechanisms in turn; current understanding of the behaviors is compared against detailed experiments and high fidelity DNS. In the second section, the uncertainty in prediction accuracy is considered; which mechanisms are poorly predicted in industry-standard Reynolds-averaged Navier–Stokes (RANS) CFD is discussed and possible improvements to the modelling are presented. Finally, designs are created to reduce loss by rebalancing the three mechanisms; performance is determined with rapid experimental test and the sources of improvement are discussed.

2 Multi-Order Methodology

A multi-order approach is used to understand the tip leakage flow structure and loss mechanisms. This allows the benefits of four different tools to be exploited to improve overall understanding. In this section, each method is described in turn, note that a scaled geometry is used for all methods, and it is representative of a rear stage of a modern aero-engine axial compressor operating at its design point. The blading style is controlled diffusion, and the unshrouded stator has a clearance-to-axial chord ratio of 1.6% and clearance-to-span ratio of 1.3%.

2.1 Rapid Test.

The Gibbons rig is a subsonic single-stage research compressor, used most recently in Refs. [8,11] and described more fully in Ref. [12]. It is built at twice engine scale and has a Reynolds number of 350,000 based on stator chord. The meridional view is shown in Fig. 2. The inlet boundary condition is set with a complete flow conditioning gauze [13], and so this single-stage rig can be considered representative of an embedded stage.

In this article the rig is used to measure the time average performance. Results from the datum design are used to determine the uncertainty of CFD predictions. And a matrix of 16 designs, with varying tip section camber distribution and tangential lean angle shown in Fig. 2, is used to improve performance by rebalancing the loss mechanisms.

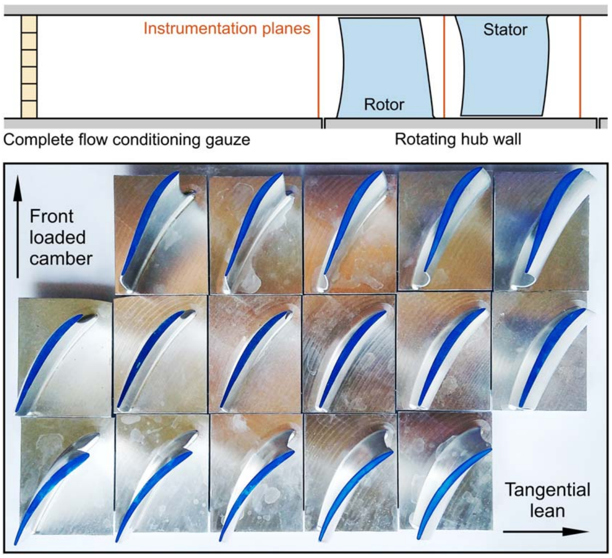

Fig. 2 Gibbons compressor rig schematic and matrix of 16 stators with varying lean and tip section camber

In order to test 16 designs as rapidly as possible, each step in the experiment has been optimized. The design process is iterative and automated to maintain the datum loading distribution with the method described in Ref. [14]. Manufacture is performed in house with custom software to generate the five-axis milling programs automatically. The rig itself has been designed to allow sectors of blades to be changed without disassembly in 15 min [15]. For each new design, a sector of eight stator blades is swapped into the rig and the central two passages are traversed upstream and downstream with a five-hole probe. This has a probe diameter to trailing edge thickness ratio of 1.0 and is moved over a grid of 49 × 25 points adaptively clustered to best resolve blade wakes and endwall boundary layers in the 0–30% span region.

2.2 Detailed Measurements.

The Freeman rig is a three-stage, four times engine scale experiment using the same datum geometry as the Gibbons at the same Reynolds number. It was previously described in Ref. [16] although the geometry has been updated to match the unshrouded stator design and clearances of the Gibbons rig. The meridional view of the new configuration is shown in Fig. 3.

In this article, the rig is used to take detailed time-resolved measurements because of its large size and low speed. The frequency range of a single miniature hot-wire resolves structures down to twice the dissipation lengthscale. The flow in the passage of stator two is traversed with 25 points from 0.1% to 30% span in the vicinity of the suction surface; Fig. 3 shows the matrix of 7 × 15 holes in the stator casing where each radial traverse is taken. Note that during an experiment all are plugged flush with the casing line except the current hot-wire location. The flow conditions within stator two are representative as they have been set by the upstream four blade rows to achieve a repeating stage configuration.

2.3 Direct Numerical Simulations.

3DNS is used to simulate the flow through the tip gap and within the blade passage down to the dissipation lengthscales. It uses the fourth-order DRP finite difference central scheme of Ref. [17] coupled with an eighth-order standard filter. It has been used for compressor applications in Refs. [18,19] where it is described in more detail. The case used in this article has been previously presented by Maynard et al. [8] where

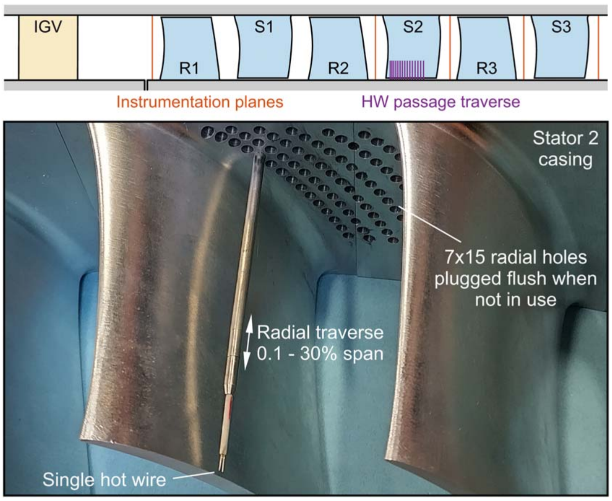

Fig. 3 Freeman compressor rig schematic and stator two in-passage traverse with single miniature hot wire

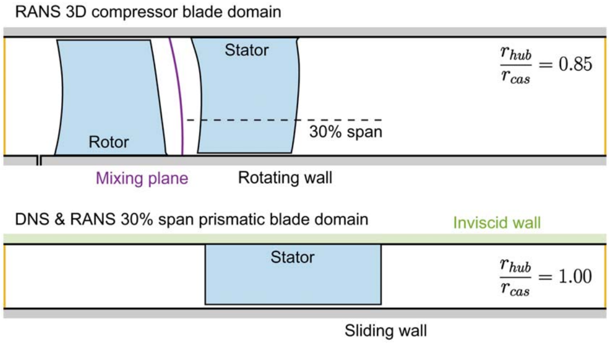

Fig. 4 3D compressor and prismatic blade CFD domains

it is referred to as the small gap 3D stator with 1.6% clearance-to-axial chord ratio. They showed that the numerical dissipation was less than 1% of the viscous dissipation, and so all scales in the flow are adequately captured.

While this method gives full knowledge of the flow without any of the issues or errors caused by turbulence modeling in RANS, it is extremely expensive. The case presented in this article is limited to a 30% span calculation on a prismatic blade geometry at a Reynolds number of 120,000 based on stator chord. Figure 4 shows the extent of the domain: the inlet and outlet boundary conditions are extended, a sliding wall with matched velocity ratio is used at the hub end and an inviscid wall is applied at the 30% span location. Even this one case with the accelerated prismatic geometry required 1.6 billion nodes and months of compute time on 5,100 cores.

This high fidelity CFD method requires realistic freestream turbulence for accurate results. In this case, the intensities and length scales are derived from experimental hot-wire traverses. These are used to inform the synthetic eddy generation process presented in Ref. [20], which applies velocity fluctuations at the inlet plane, which develop turbulence to the expected intensity upstream of the row. The outcomes are matched radial profiles of velocity, flow angle, and turbulence spectra at the stator leading edge in both the Freeman compressor rig and this DNS calculation. Two figures are shown in Ref. [8] showing agreement in this location for this same DNS case.

2.4 Reynolds-Averaged Navier–Stokes Simulations.

TURBOSTREAM [21] is a 3D multi-block structured second-order finite-volume RANS solver used to predict the flow in both the datum geometry and the matrix of 3D stator designs shown in Fig. 2. Two domains are used in this article and both are shown in Fig. 4: The first models the full two rows of the Gibbons compressor rig stage with all inter-platform gaps, tip clearances, and fillets resolved. The second is a prismatic geometry extending over 30% of the span closest to the hub for direct comparison with the DNS calculations. The two cases differ in their hub-to-tip radius ratios; the full 3D compressor blade domain has a hub-to-tip radius ratio of 0.85, while the prismatic blade domain has a value of 1.00 and is effectively a cascade with moving endwall.

Industry-standard grids are used with the Spalart–Allmaras turbulence model [22], one million cells per passage, and well resolved walls with $y^+ < 1$. Point transition is specified at 20% of suction surface chord as predicted by MISES [23] and confirmed with oil flow visualization. The code was originally validated in Ref. [21] and was recently used in Ref. [7] to study tip leakage flows in compressors and is successfully compared to experiment.

These simulations only take 15 min to run a single stage on a single NVIDIA A100 graphics card, and so hundreds of runs become practical. In this article, RANS is used iteratively to automate the design process, each new design takes five iterations to converge. The same 16 blade matrix experimentally tested in the Gibbons compressor can be covered with a finer resolution 55 blade matrix. For research purposes, TURBOSTREAM enables investigation of different modeling parameters to improve prediction, and in particular, the rate of turbulence production can be specified locally within different regions of the domain.

3 Loss Mechanisms

In this section, our current low-order understanding of tip leakage flow is compared against DNS and detailed experimental measurements. Although the kinds of tip leakage calculations and models presented in Refs. [3,1,4] are no longer useful for advanced design, this model of the flow is still something engineers hold in their minds when interpreting the 3D CFD calculations. Extracting useful parameters or anticipating the direction of design changes relies on a shared low-order understanding that this article is aiming to update.

3.1 Flow Structure.

Figure 5 shows a slice through the DNS calculation where the flow is colored by dissipation coefficient and by entropy function. These visualizations serve two purposes: they indicate regions where loss is generated and regions where the loss is ultimately convected to. In these images, the flow is pulled from left to right and accelerated into the gap. It then immediately separates from the pressure side corner of the blade, and this bubble sheds and begins mixing within the gap.

As the flow exits the gap on the suction side, a shear layer is formed, which also sheds and mixes the leakage flow with the mainstream. Note that there is no discernible tip leakage vortex, this is consistent with the work of Maynard et al. [8] who showed that the instantaneous vorticity in the fine scale eddies of the shear layer are more significant than the vorticity that appears in the time-averaged flow solution.

Close to the hub wall there is an increased dissipation and entropy where the shear of the rotating endwall is acting on the flow, and in this image, this is in the left to right direction. The greatest mismatch in velocity between flow and the endwall occurs after mid-pitch once the leakage jet has undergone some mixing and has decelerated.

Figures 6(*a*) and 6(*b*) show the distribution and initial trajectory of the flow as it exits the gap on the suction side. In Fig. 6(*a*), the leakage mass flow is plotted against chord from leading edge (LE) to trailing edge (TE) for the DNS calculation, the RANS simulation, and also the classic tip leakage model proposed by Rains [2] and presented in Storer and Cumpsty (S&C) [3]. In this model, a discharge coefficient of 0.88 can be used to match the total leakage mass flow. In Fig. 6(*b*), the yaw angle of the

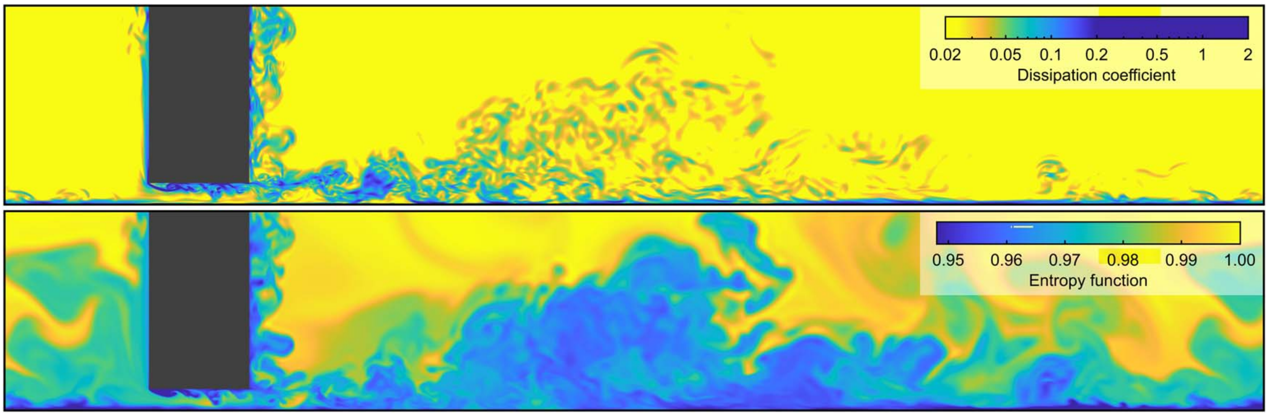

Fig. 5 Contours of entropy function and dissipation coefficient at 50% chord through instantaneous DNS solution

leakage jet is plotted; a value greater than 90 deg indicates a component of velocity in the negative axial direction. Significant discrepancy is seen in the predictions of the S&C model, up to 20 deg in some regions of the blade.

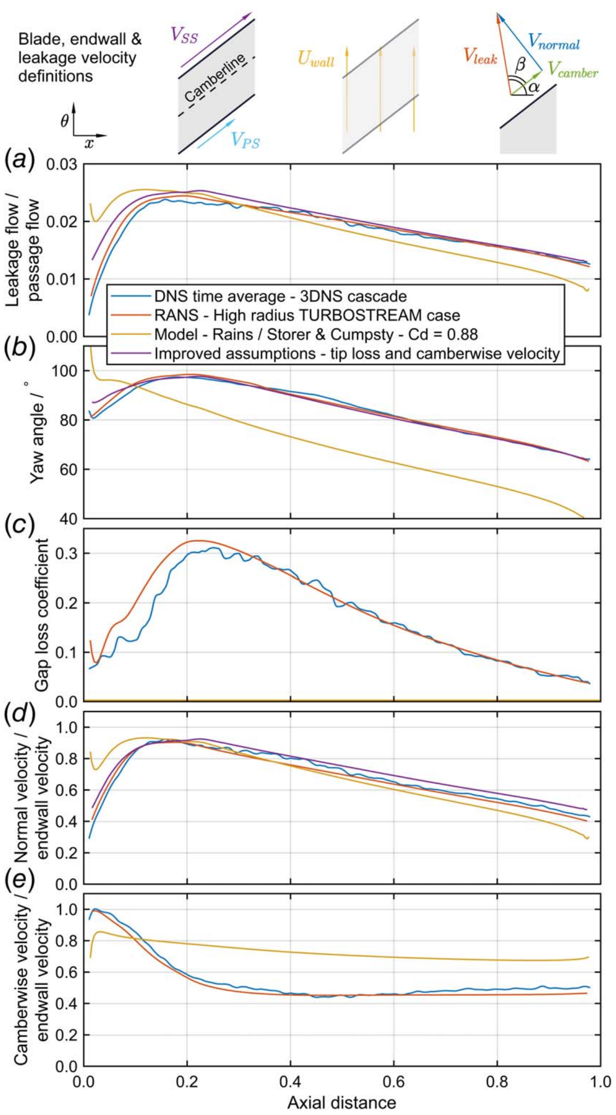

Fig. 6 Mass-averaged properties across SS gap including leakage rate and initial trajectory, stagnation pressure loss within the gap and jet velocity components

There is evidently physics of the flow that is not adequately captured in the model's assumptions, and this article will show two features that can account for this difference: First, the loss generated within the gap itself, and second, the trajectory of the flow before it enters the gap on the pressure side. It is important that these are understood in the future as they could cause potential issues or provide opportunities for design improvement.

3.2 Gap Separation Loss.

The flow within the tip gap itself is far from isentropic as usually assumed. Figures 1 and 5 show regions of significant dissipation within the gap itself, and in terms of magnitude, these are the highest in the entire passage. Figure 6(*c*) shows the loss coefficient calculated from the DNS between the pressure side and suction side of the tip gap as a function of axial distance on the blade. Close to peak suction, this loss is 30% of the inlet dynamic head into the blade row. Depending on the gap size and blade aspect ratio, this component of loss makes up 5–10% of the total passage loss.

The effect of this loss coefficient on the leakage flow trajectory can be calculated by considering the two components that make up the leakage velocity, V_{camber} and V_{normal} defined in Fig. 6. If the flow through the gap is assumed to be isentropic as in S&C, the magnitude of the leakage velocity V_{leak} is equal to the magnitude of the suction surface velocity V_{SS}. However, when losses in stagnation pressure occur within the gap V_{leak} will be reduced. Assuming incompressible flow and unchanged V_{camber}, the effect on V_{leak} can be calculated with Eq. (1).

$$V_{\text{leak}}^{2} = V_{\text{camber}}^{2} + V_{\text{normal}}^{2} = V_{\text{SS}}^{2} - \frac{P_{0,\text{PS}} - P_{0,\text{SS}}}{0.5\rho} \qquad (1)$$

$$\beta = \arccos\left(\frac{V_{\text{camber}}}{V_{\text{leak}}}\right) \qquad (2)$$

Equation (2) shows the calculation of the leakage trajectory angle relative to the blade surface β. By using these two equations, it can be seen that losses within the gap will reduce the leakage flow trajectory relative to an isentropic gap. Correcting this assumption highlights a future opportunity, design can be undertaken specifically to reduce the gap separation loss mechanism, as in the test matrix in this article.

3.3 Mainstream Mixing Loss.

As the jet exits the gap on the suction surface, it is misaligned with the mainstream flow. Figures 1 and 5 show dissipation close to the suction side, which is most intense between 25 and 60% chord at a spanwise location between 0.2 and 1.8 gap heights. These are the regions of most significant velocity misalignment shown in Fig. 6(*b*). In this figure, the calculation of the leakage flow trajectory in the S&C model shows significant error in angle, and this would ultimately feed through to

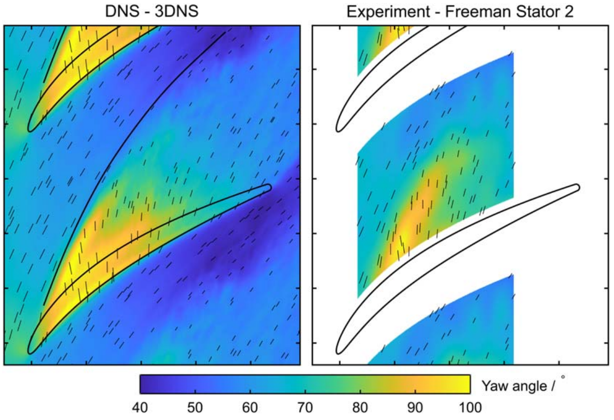

Fig. 7 Trajectory of flow at 50% of gap height from DNS time average and Freeman rig hot-wire experiment

an error in the mixing loss calculation and could be caused by either of the two velocity components V_{camber} and V_{normal}.

The normal component of the velocity, V_{normal}, is well represented by the S&C model and is plotted in Fig. 6(*d*). The static pressure difference across the blade tip is solely responsible for accelerating the flow through the gap and determines the shape of the velocity distribution.

However, the camberwise velocity, V_{camber}, plotted in Fig. 6(*e*) is not well represented by the S&C model, which sets it to the isentropic velocity on the pressure side of the blade. Close to the leading edge, the model predicts a reduced camberwise velocity, while in the rear 90% of the blade, it is increased by up to 62%. This has a direct impact on the trajectory relative to the blade surface β plotted in Fig. 6(*b*), where over the rear 90% of the blade chord the trajectory in the model is too low.

The time average of the DNS calculation can be used to explain why the camberwise velocity component differs from the assumption. Figure 7 shows the yaw angle of the flow on a slice halfway between the endwall surface and the gap. The flow in this region of the passage is stratified by the presence of the endwall, and it ensures that any spanwise velocity components are small compared to the axial and tangential values. In this plane, the maximum spanwise velocity is less than 15% of the suction surface velocity. This means that the flow is effectively constrained to remain in its original plane, and so blade-to-blade cuts through the domain can be used to see the behavior of the whole flowfield.

Figure 7 shows the local flow velocity and trajectory in the time-averaged DNS flow field with short black lines. It also shows a longer solid line, which is a streamline integrated from the suction surface close to the leading edge. The leakage flow causes significant blockage within the passages, effectively changing its shape in this plane. Note that the streamline from the leading edge cannot be crossed by the incoming flow as the spanwise velocity is constrained.

The blockage turns the flow toward the tangential direction, funneling it through the next tip gap. This flow turning that occurs outside of the gap reduces the camberwise velocity component V_{camber} relative to the flow that is attached on the pressure side of the blade V_{PS}. The effect is only caused once the blockage begins to influence the direction of the incoming flow, and the underprediction of yaw angle shown in Fig. 6(*b*) occurs from 10% chord onward.

Again, improved understanding around this assumption is a design opportunity, and by manipulating the trajectory of the flow at entrance to the gap, the trajectory at outlet can be affected, and the mixing loss with the mainstream can be reduced. In the test matrix considered in this article, front and rear loading the blade tip sections can manipulate the effective shape of the passage beneficially.

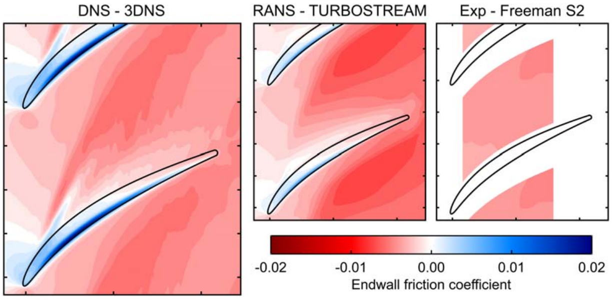

Fig. 8 Frictional shear stress on endwall in the tangential direction from DNS, RANS, and Freeman rig experiment

3.4 Endwall Shear Loss.

Endwall loss is created by a mismatch in velocity between the rotating hub wall and the fluid in the passage. Figures 1 and 5 show that the most significant dissipation occurs at less than 20% of the gap height from the wall. Figure 7 shows the flow in the endwall boundary layer at inlet moving with a yaw angle of 70–80 deg, and this causes minimal dissipation as it is well aligned with the endwall direction. At mid passage and at the rear of the row, the yaw angle is reduced down to 40 deg by two mechanisms. First, the tangential velocity is reduced by the turning of the blades and the cross-passage pressure gradient. Second, losses within the gap and mixing with the mainstream decelerate the leakage flow; stagnation pressure is reduced while static pressure is maintained by the bulk flow.

The motion of the hub wall acting on the almost stagnant fluid on the pressure side of the passage causes dissipation and loss. Figure 8 shows the friction coefficient, and it is the nondimensional shear stress in the tangential direction, plotted on the hub endwall for the RANS, the time-averaged DNS flowfield, and the detailed experiments conducted within the passage of Stator 2 in the Freeman rig. These experiments are able to resolve the shear stress components by measuring the velocity in the tangential direction at 0.1% span. The red regions show where the tangential velocity of the flow is less than that of the hub wall and the flow is sheared. The most significant regions are under the leakage jet, at mid passage, after it has mixed with the mainstream flow and the stagnation pressure has been reduced. Not only is this shown clearly in the DNS and RANS data but also the measured region in the Freeman shows elevated shear closest to the pressure side at the rear of the passage.

The DNS results plotted in Fig. 8 also show another region of high shear but in the opposite direction. The blue regions are where the tangential velocity is higher than the hub velocity and work is being extracted from the flow; this only occurs locally where the flow is accelerated within the tip gap itself. The pressure difference of the blade, combined with the reduction in effective area caused by the pressure side edge separation bubble visualized in Fig. 5, increases the tangential velocities to this level.

3.5 Double Leakage.

Double leakage is the phenomena where flow that has passed through one tip gap passes across an entire pitch and goes through the neighboring gap. While not a loss generating mechanism in its own right double leakage can have a significant effect on the trajectory of the leakage flow and therefore the balance of loss mechanism. If this occurs, the stagnation pressure of the flow at the gap entrance on the pressure side can be reduced relative to the usually assumed freestream value. Khalid et al. [24] described this effect and how a reduced stagnation pressure will reduce the trajectory, the angle β of the leakage flow, when the flow subsequently exits on the suction side of the gap.

In reality double leakage is always present to some extent as the flow that is closest to the endwall is travelling at 90 deg, being dragged by the spinning hub. The effect can be quantified by the mass flowrate that passes through a second gap after it leaves the

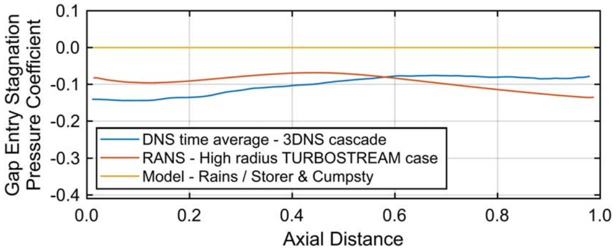

Fig. 9 Stagnation pressure at pressure side gap entry

first. In this article, streamlines are tracked from the gap exit on the suction surface of one blade. The fraction of mass flow passing through the neighboring gap can then be calculated, and for the DNS calculation, this is 17% of total tip leakage flow.

The effect of this on the stagnation pressure at gap entry can also be quantified and is plotted in Fig. 9. Both DNS and RANS calculations have a stagnation pressure that has been reduced from the freestream value by 10% of the inlet dynamic head. It has a weak effect in this design, but other cases will have larger values, and Khalid et al. report 40% stagnation pressure reductions in Ref. [24]. The S&C model neglects this effect, and the zero gap entry stagnation pressure coefficient shown in Fig. 9 is therefore responsible for a small error in the trajectory prediction.

3.6 Improved Understanding. This section of this article has shown three unappreciated mechanisms that are critical to the understanding of tip leakage loss. First, the gap loss coefficient is significant, and it can affect the initial trajectory of the leakage jet as it exits the suction side of the gap. Second, blockage caused by the leakage jet itself can influence the camberwise velocity component, also affecting the trajectory. Third, endwall loss is greatest in the pressure side of the passage and is caused by a mismatch in velocity of the stagnant flow in the mixed leakage jet with the relatively fast endwall surface.

The effects on the trajectory can be tested by revisiting the S&C model of Ref. [3] and replacing the original assumptions with the gap loss coefficient and actual camberwise velocity. Curves are added to the plots of Figs. 6(*a*) and 6(*b*) in purple; accuracy has been improved in the distribution of leakage mass flow and the yaw angle is now within ±1 deg of the DNS results. This shows that it was only these two pieces of information that were missing from the original model of [3] for almost perfect agreement.

The endwall loss mechanism is tested by investigating regions of velocity mismatch, Fig. 10 shows the endwall shear coefficient calculated from the instantaneous DNS using Eq. (3).

$$C_{\text{shear}} = \frac{\left(V_x{}^2 + (V_\theta - U_{\text{wall}})^2\right)^{\frac{3}{2}}}{U_{\text{wall}}{}^3} \tag{3}$$

The location and structure of the greatest regions of velocity discrepancy close to the endwall in Fig. 10 match the regions of high dissipation shown in Fig. 1. The formulation of the coefficient as a velocity cubed is directly analogous to the dissipation in an attached boundary layer, which is proportional to the freestream velocity cubed as described in Ref. [1].

4 Prediction Uncertainty

Figure 11 shows the stagnation pressure field at stator exit from a five-hole probe traverse in the Gibbons rig and the RANS calculation run with the Spalart–Allmaras turbulence model. In this section, three aspects of uncertainty are considered in the RANS prediction: First, uncertainty in the size of the separation bubble on the tip of the blade; prediction accuracy here is essential to set the initial jet trajectory. Second, shortcomings in the prediction of the mixing rate in RANS CFD and how this can be improved with information about the physics taken from the DNS calculation. Third, discrepancies in the work input on the flow by relative endwall motion and its secondary effect on the final leakage trajectory.

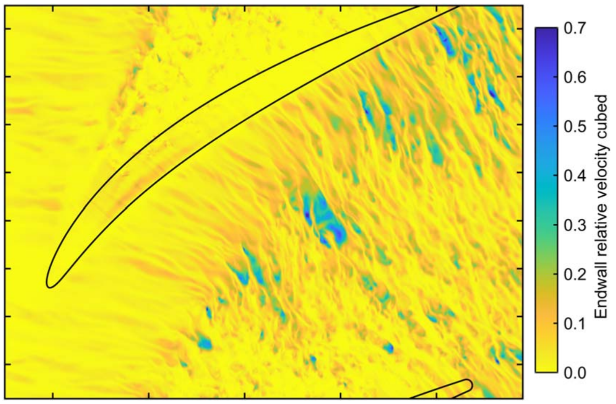

Fig. 10 Velocity relative to endwall cubed at 17% gap height from instantaneous DNS using Eq. (3)

4.1 Initial Trajectory. All of the calculations show that separation in the gap begins from the pressure side edge of the blade tip. Low-order models of the leakage flow often take this into account with a reduced "effective gap" that deals with the blockage of the separation. Whether this flow reattaches on the tip of the blade has been debated in the literature. The recent work of Maynard et al. [8] showed that their 3.2% gap to chord DNS case still reattached on the tip itself, a value greater than previously reported.

Figure 12 shows surface flow visualization performed in the Freeman rig, with two colors of fluorescent pigment suspended in silicone oil. The photograph taken under UV light shows the structure of the flow passing through the tip gap when the rig is at its design point. Close to the pressure side, the orange pigment shows the extent of the separation bubble, while green shows where the flow reattaches on the suction side three quarters of the tip thickness. The other two images show surface limiting streamlines integrated from the time-averaged DNS and RANS calculations. The same colors show the separation occurring at the sharp edge on the pressure side and reattachment on the tip itself in a similar location.

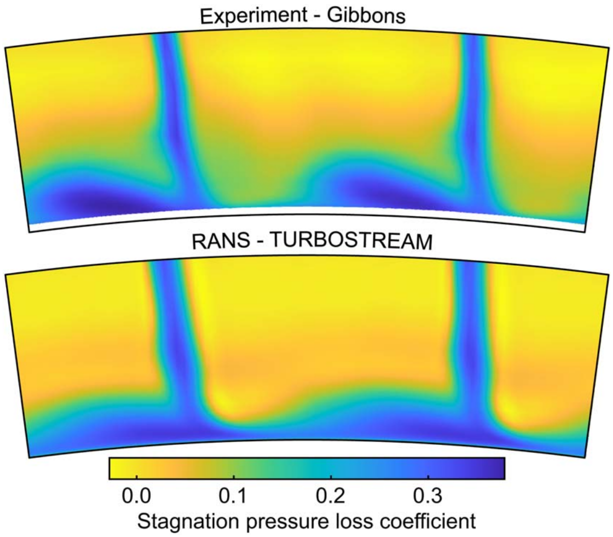

Fig. 11 Stagnation pressure loss at stator exit from both Gibbons rig experiment and RANS

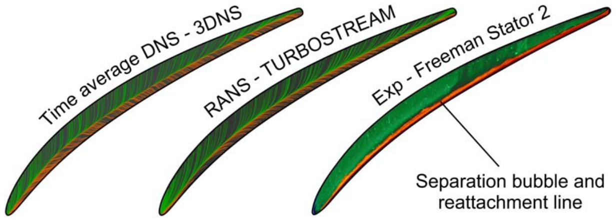

Fig. 12 Limiting surface streamlines and oil flow visualization showing separation bubble reattachment

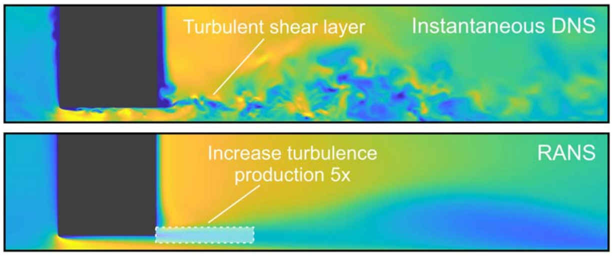

Fig. 13 Contours of velocity showing mixing of the leakage jet in turbulent shear layer at 30% chord

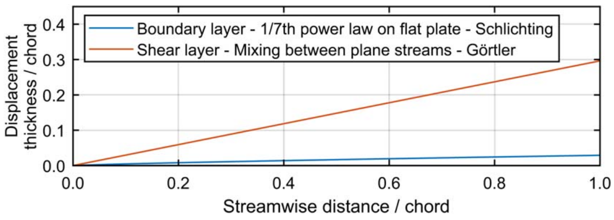

Fig. 14 Correlations for boundary and shear layers

The flow physics in the gap itself is well modeled by the RANS calculation, and so the loss coefficient within the gap and the initial trajectory of the leakage flow at gap exit are expected to be correct. Figure 6 shows excellent agreement for both this industry-standard RANS calculation and the high fidelity DNS calculation. This region of the flow is therefore not responsible for the discrepancies shown in Fig. 11.

4.2 Mixing Rate. Although the initial trajectory of the leakage flow as it leaves the tip gap is well predicted by RANS, its final location at the blade row exit in Fig. 11 is not. In that figure, the flow is coming through the blade tips from left to right at the hub end; the loss cores on the endwall have travelled across most of the pitch. The major discrepancy can be seen in the shape of the loss core, and in the RANS prediction, it is flatter and closer to the wall and joined to the wake of the neighboring blade on the right.

Figure 13 shows velocity on axial cuts through both the RANS and DNS calculations. The DNS is shown at an instantaneous snapshot in time, and the RANS is a steady simulation. In the DNS case, it is clear that there is no discernable tip leakage vortex, and in fact, the flow is mixed rapidly by a shear layer composed of fine structures shed from the suction surface corner of the gap along the entire chord of the blade. Rapid turbulent mixing ensures that the high loss region of the flow does not make it as far across the pitch toward the next blade's pressure side as it does in the RANS plotted in Fig. 13.

The root cause of this discrepancy comes from the turbulence modeling in the RANS. The Spalart–Allmaras model, like most other models, is tuned to experiments performed on boundary layers. However, boundary layers and shear layers, like those present in this flow structure, behave very differently. Figure 14 shows this difference with two correlations for the growth of both wall bounded layers and unbounded shear layers from Ref. [25]. When evaluated over the length of a blade chord, the boundary layer is expected to grow 3.8% of chord in height, and over the same distance, the shear layer grows 30% of the chord in width.

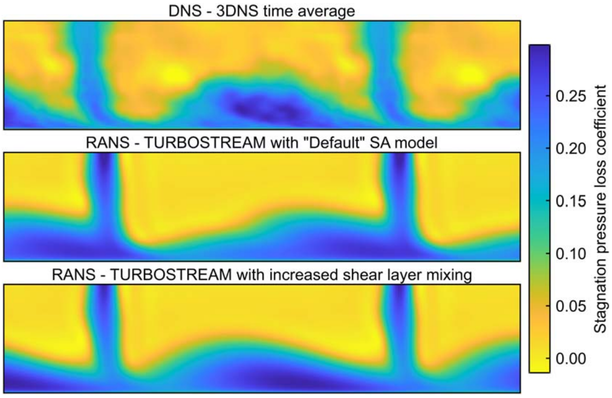

Fig. 15 Position of leakage flow at stator exit with default and tuned turbulence models compared to DNS

Because of this factor of eight difference in the growth rate, it is clear that the mixing process in the RANS calculation is underpredicted. In TURBOSTREAM, it is possible to tune the turbulence model locally and increase mixing, and so a zone of five times increased turbulence production[2] is drawn around the region where the shear layer initially forms and the mixing rate is greatest. Figure 13 shows the zone centered on the suction surface edge of the blade tip, while the length of the region is the same as the tip thickness and its height is the same as the gap height. The zone extends from leading to trailing edge. With this modification, momentum transport between the leakage jet and the mainstream increases. In addition, the jet has a lower velocity after rapid mixing and is overturned back toward the suction surface as the cross-passage pressure gradient has a more significant effect.

Figure 15 shows the results from this modification. At the top is a cut at stator exit from the time-averaged DNS showing entropy loss coefficient. The center shows the same RANS calculation of Fig. 13 with the default turbulence model settings. The bottom is RANS with the local increase of the turbulence production term by a factor of five. There is now much closer agreement between the modified RANS and the DNS calculation, both of which look most similar to the experimental results presented previously in Fig. 11. Note that Figs. 11, 13, and 15 are the only RANS cases to be run with the default turbulence model settings, and every other result in this article is obtained with the modification to increase mixing in the shear layer and improve the agreement with both experiments and DNS.

4.3 Endwall Work. In a cantilevered stator, the spinning hub wall mostly puts work into the flow by increasing its tangential velocity in the absolute frame. Figure 15 shows good trajectory prediction in the 5–15% span region with the tuned turbulence model. However, in the 0–5% region, the prediction of the RANS could still be improved. When compared to the DNS, the flow in the RANS is being dragged from left to right across the passage and under the next blade row by the motion of the hub wall. This is confirmed in the plots of Fig. 8 where the RANS case has increased shear work by 20% over most of the passage.

Figure 8 also highlights another shortcoming of the RANS prediction under the tip gap itself. The strong region of blue in the

---

[2] A range of factors between 1 and 20 were investigated, and the multiplier of five was found to give the best agreement.

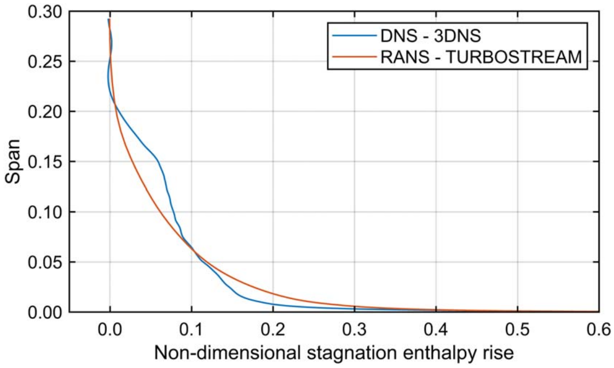

Fig. 16 Work input by rotating endwall in DNS and RANS

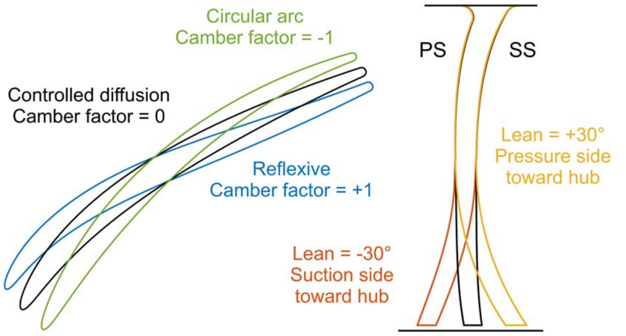

Fig. 17 Lean and tip camber geometry modifications

DNS shows work being extracted from the flow by the wall that is lower in the RANS by a factor of three. This is caused by the large-scale structures shed by the bubble on the pressure side edge of the tip shown in both Figs. 5 and 13. In the DNS calculation, the structures increase the rate of momentum transport close to the hub endwall surface and therefore the magnitude of shear stress on the wall. In the case of the RANS, the separation bubble is modeled as a steady feature and so the turbulent viscosity on the opposing endwall surface is too low for the correct shear stress to be predicted.

The work input in this stator row is quantified by the stagnation enthalpy rise nondimensionalized by the endwall speed squared. Figure 16 shows the work input for both the DNS and tuned RANS calculations. Below 6% of the span, the RANS shows an increase in stagnation enthalpy relative to the DNS calculation, while values are reduced further from the hub. As well as the work input being higher for the RANS calculation, the rate of mixing in the spanwise direction is lower. This is an issue for the prediction of this single row, but it will also cause issues in multistage calculations where the buildup of high temperature near the endwalls is overpredicted and unphysical [26].

In this region of the flow, the boundary layer is skewed and three dimensional, and it also interacts with the unsteady flow features within the gap and outside of it. This is outside the boundaries of the original data that the Spalart–Allmaras turbulence model is based on; flow with a collateral freestream and boundary layer. To improve the rate of mixing and the shear work done by the endwall, turbulence modeling needs a more bespoke approach.

5 Reduced Loss Blading

The location and trajectory of the leakage jet depends upon the shape of the static pressure distribution carried by the tip of the blade. If the pressure distribution is front loaded, then the leakage flow has a greater angle mismatch concentrated in the front part of the chord, and this affects the three loss generating mechanisms differently. In this section, blade loading is independently controlled through modification of two geometrical parameters: lean in the tangential direction and the distribution of camber in the tip sections of the blade. They are both varied in combination and applied as deltas to the datum stator blade. All cases have been automatically redesigned to give the same turning at exit of the row and are interchangeable with the datum design in a multistage machine.

5.1 Lean and Camber Matrix. Figure 17 shows three blade tip sections in the matrix with varying camber distribution as well as three axial sections with varying tangential lean. Lean angle is varied from −30 deg, where the suction surface makes an acute angle with the hub, up to +45 deg in the more conventional direction. The red and yellow blade sections show ± 30 deg lean angles relative to the black datum geometry. The camber distribution is quantified by the camber factor, a linear scaling of the nondimensional camber distribution between the datum and a circular arc blade shown in green, and these have the values 0 and −1, respectively. It is then possible to extrapolate this treatment further in both directions, down to a camber factor of −1.5 and up to a factor of 1, where the camber distribution becomes reflexive as shown by the blue blade section.

The modifications to the camber distribution and the lean are applied only to the lower sections of the blade with a smooth transition at midspan; therefore, the 50–100% span sections of the blade are similar. The 16 blade designs tested in the Gibbons compressor rig are shown in Fig. 2, and a larger matrix of 66 cases is investigated using RANS.

Figure 18 shows the predicted entropy loss coefficient integrated between 0% and 30% span for the test matrix. These TURBOSTREAM solutions indicate that loss can be reduced by 10% if the designs are front-loaded relative to the datum. The positive camber distribution pushes peak suction forward, as does positive lean. Lean is able to achieve this without changing the stagger of the blade. However, the camber distribution and the stagger are inherently linked; front loading reduces the mean angle of the blade tip section. Designing with these two parameters independently allows the leakage jet angle to be modified relative to both the mainstream flow angle and the direction of the spinning hub.

5.2 Experimental Test. Figure 19 shows the measured loss coefficient at stator exit. The wide range of lean angles and camber distributions investigated in this article show how the position and intensity of the high loss leakage flow can be controlled. Rear loaded designs with negative lean and circular arc camber distributions show the highest loss where the leakage flow collects in a core of fluid that sits at mid passage. Front-loaded designs with positive lean show the best overall performance with the leakage flow passing close to and even under the pressure surface of the neighboring blade.

Figure 19 shows that it is possible to manipulate the balance of the three tip loss mechanisms with both kinds of geometry

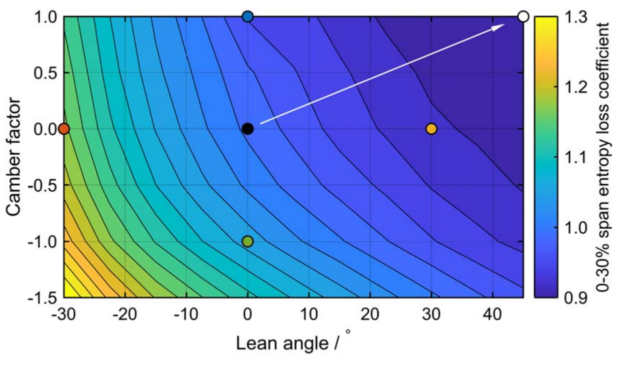

Fig. 18 Total leakage losses with lean and camber

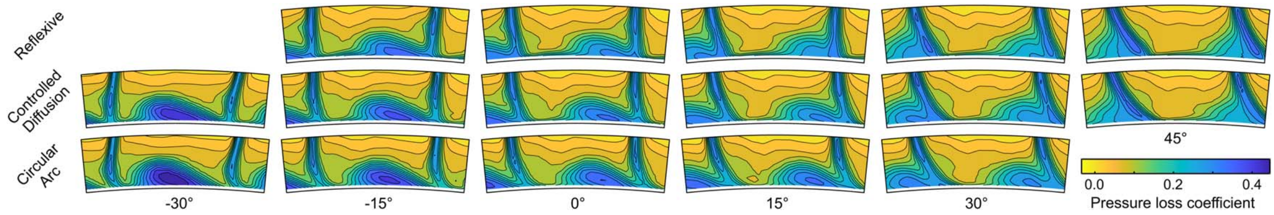

Fig. 19 Experimental traverses showing stagnation pressure loss coefficient at stator exit for test matrix

change. Equivalent mainstream mixing loss components can be achieved with either positive lean or a reflexive camber distribution. Comparing the traverses diagonally from top left to bottom right shows similar intensities of loss cores at mid passage.

However, the endwall loss does not vary in the same way, and the traverse allows access into the hub endwall boundary layer and local differences can be determined. The contours close to the suction side and endwall indicate that the cases with circular arc camber distributions are performing better in this region. This means that the reflexive 0 deg lean design might have a similar loss core to the circular arc +30 deg lean design but a different endwall shear loss component. This is because a leakage jet with an absolute yaw angle closer to 90 deg will have reduced endwall shear acting on it. Circular arc blades have an increased stagger and mean angle of the blade surface, and so the angle of leakage jet is increased in the absolute frame.

Figure 20 shows the experimentally measured integrated loss coefficient between 1.9% and 30% span. Loss is continually decreasing with increasing lean and increasing camber factor with no sign of an optimum anywhere close to the limits of the data collected in this matrix. This experimental data show that significant improvements in the leakage losses are possible and that relative to the datum the best design in this set has reduced loss by 18%. Note that the RANS stagnation pressure loss coefficients integrated over the same spanwise region predicted improvements of 13% for the reflexive 45 deg lean design and follows as similar trend as shown in Fig. 18.

5.3 Loss Breakdown. Although differences in the structure can be seen in the experimental traverses of Fig. 19, it is not possible to rigorously breakdown the changes in loss into their component sources. Loss occurs sequentially as the leakage jet passes through one blade tip, mixes with the mainstream, and interacts with the endwall; by the time it reaches the traverse plane at stator exit, it is well mixed. In this section, the RANS calculations are used to understand the changes occurring in the flow structure and the different sources of loss across the test matrix.

The domain is split into four different volumes, and local loss coefficients are calculated for the three tip leakage loss mechanisms and the remainder, which is predominantly attached loss on the blade surface. Figure 21 shows this breakdown for the matrix of different designs. The axes are the same as shown in Fig. 18; along the *x*-axis, lean is increasing in the positive direction to the right, and the *y*-axis shows front-loaded tip sections with reduced stagger. The color scale is identical across all four plots, showing that larger absolute reductions are possible in the gap separation and mainstream mixing loss mechanisms. For reference, the relative fractions of each component for the datum design are given in Table 1.

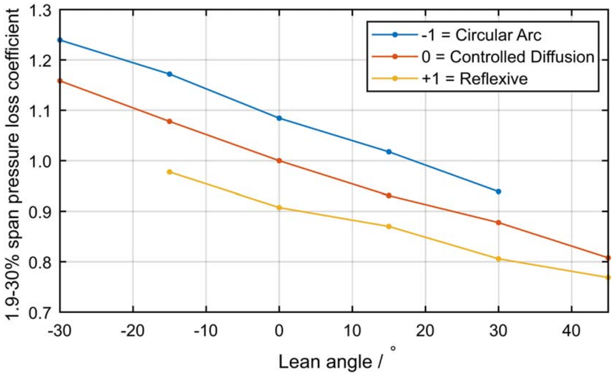

Fig. 20 Experimentally measured loss coefficients for test matrix between 1.9% and 30% span

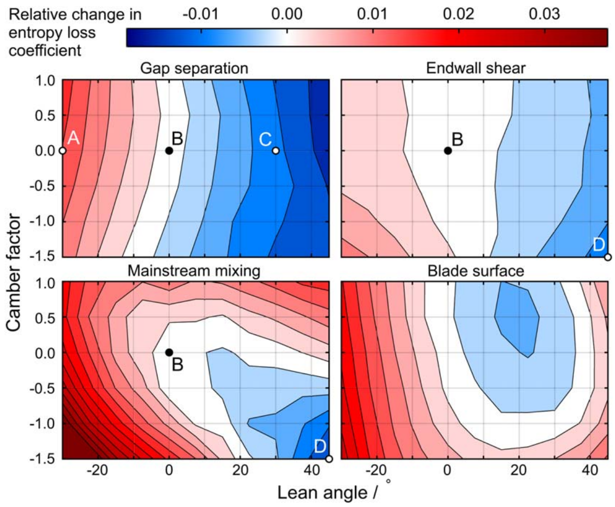

Fig. 21 Breakdown of entropy loss components with lean and camber, changes relative to datum total loss

The *gap separation loss* component, caused by mixing out of the separation bubble, is most sensitive to lean angle, and Fig. 21 shows contours approximately parallel to the lean angle of the different designs. This loss mechanism is entirely determined by the sharpness of the pressure side edge of the blade. Figure 22 shows slices taken at 35% chord through three different designs with lean angles of −30 deg, 0 deg, and +30 deg. The sharpest blade edge in design A causes a larger separation bubble that blocks a larger fraction of the gap height. The increased velocity nonuniformity increases mixing losses within the gap. For design C, with improved gap separation losses, the bubble is significantly reduced and now blocks less than 5% of the gap.

The mixing losses within the gap are quantified with the gap velocity coefficient given in Eq. (4). The +30 deg lean design has a 14% lower mass-average gap velocity coefficient than the datum design.

$$C_{\mathrm{gap}} = \frac{V_{\mathrm{peak}}^{2}}{U_{\mathrm{wall}}^{2}} \tag{4}$$

Table 1 Relative loss fractions in datum design 0–30% span

Gap separation	Mainstream mixing	Endwall shear	Blade surface
0.11	0.32	0.11	0.46

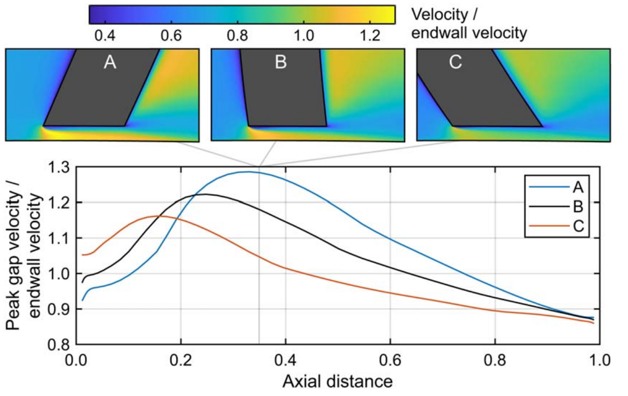

Fig. 22 Peak velocity distribution within the gap for cases A, B, and C, contours plotted at 35% chord

The *mainstream mixing loss* component, caused by the mismatch in jet leakage velocity and local suction surface mainstream velocity, is reduced with positive lean and negative camber factor. The case with the least mainstream mixing loss is marked as design D on Fig. 21. This is because it minimizes the velocity mismatch between the leakage jet and the mainstream flow in both the streamwise and normal directions. This can be quantified with a mixing coefficient as in Ref. [1,3].

$$C_{\mathrm{mix}} = \frac{V_{\mathrm{normal}}^2 + (V_{\mathrm{camber}} - V_{\mathrm{SS}})^2}{U_{\mathrm{wall}}^2} \tag{5}$$

The chordwise distribution of the velocity mismatch from Eq. (5) is shown in Fig. 23. The majority of the benefit is through a reduction in the normal velocity component, and this is especially important in the 10–62% chord regions where most of the leakage mass flowrate is concentrated. Design D achieves this reduced mixing loss even though the absolute trajectory of the leakage flow is increased due to the increased stagger of the negative camber factor tip section.

The *endwall shear loss* component, caused by a mismatch in the jet leakage velocity and the endwall velocity, is reduced with either positive lean or negative camber factor. Case D, from Fig. 21, is a design with +45 deg lean and −1.5 camber factor. Endwall shear loss depends on the velocity mismatch cubed, and this is calculated for design D using Eq. (3) and plotted in Fig. 24. The difference is also plotted relative to the datum design B, which shows that the velocity of the flow is more closely aligned to the endwall. A large region of velocity mismatch over the first 60% of chord is eliminated, and the intensity of the velocity mismatch in the rear of the passage near the pressure side is also reduced. Integrated over the whole of the endwall surface, the velocity relative to the endwall cubed is reduced by 8%. The reason this corner of the design space has the lowest endwall shear loss is threefold.

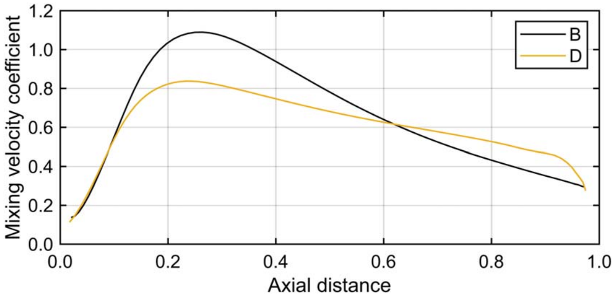

Fig. 23 Leakage jet velocity difference relative to suction surface velocity for cases B and D from Eq. (5)

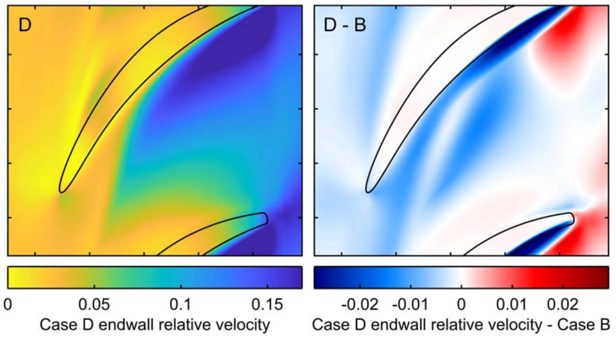

Fig. 24 Velocity relative to endwall cubed at 17% gap height for case D and differences between D and B

First, positive lean reduces gap separation losses. Equations (1) and (2) showed that reducing the stagnation pressure loss within the gap increases the initial trajectory of the leakage flow β. This sets up a jet with an increased yaw angle in the absolute frame and ultimately a tangential velocity more closely matched to the endwall. Second, lean front loads the pressure distribution at the tip section. This causes an increased proportion of the leakage flow to pass over the blade tip closer to the leading edge. In this region, the blade has an increased local camber angle, and so even with the same value of blade relative angle β, the angle of the leakage flow in the absolute frame is higher. Finally, a rear loaded camber distribution, such as a circular arc camberline, increases the stagger of the tip blade section. Again, the average tip camber angle is increased and the leakage flow also has an increased yaw angle.

The *blade surface loss* shows an optimum with increased lean and positive camber factor. Blade profile losses are reduced by front loading the pressure distributions, resulting in thinner and healthier boundary layers at the trailing edge. But too much lean can increase profile loss again, and the transverse pressure gradient contracts the boundary layers in the mid sections and increases downstream mixing losses [14]. Ultimately the best overall blade design balances reductions in the three leakage loss mechanisms with that of the blade surface loss.

5.4 Velocity Mismatch. The three loss generating mechanisms are all driven by mismatches in velocity. The separation bubble in the tip gap causes blockage, over acceleration of the flow, and subsequent mixing. As the flow exits the gap relative to the suction surface, it has a deficit of velocity in the camberwise direction and a surplus in the normal direction, and this drives a turbulent shear layer. The flow at mid passage is decelerated relative to the endwall travelling in the tangential direction, and loss is created in the 3D boundary layer.

It is possible to correlate the extracted loss components of Fig. 21 with the coefficients of velocity mismatch introduced in this article. Figure 25 shows that three parameters: First, the mass-average gap

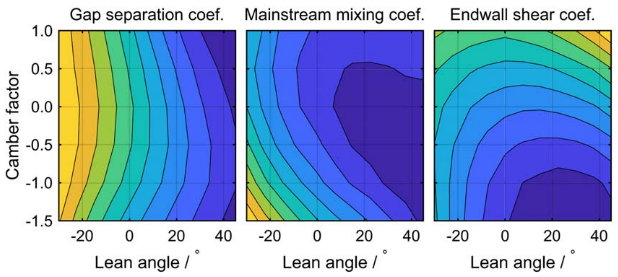

Fig. 25 Average velocity coefficients calculated for all designs using Eqs. (4), (5), and (3)

separation coefficient from Eq. (4) is plotted for all designs, and this correlates extremely well with the loss breakdown and shows the best designs with positive lean and camber factor. Second, the mass-averaged mainstream mixing coefficient from Eq. (5) also successfully maps the loss trends across the design space. Third, the area-averaged endwall shear velocity coefficient from Eq. (3) correctly identifies positive lean and negative camber factor as the region of lowest endwall shear loss. Although this last component is not perfectly aligned with the results of Fig. 21, it is likely that this proxy is closer to the truth. Recall that the prediction of loss in this 3D boundary layer is severely limited by the turbulence model in the RANS. Inspecting again the experimental results of Fig. 19 shows that the circular arc designs are indeed superior to the reflexive when it comes to endwall shear loss just as shown in Fig. 25.

6 Conclusion

This article has shown that it is essential to combine both standard and high fidelity CFD with standard and high fidelity experiments if our understanding of tip leakage flows is to be improved. Three distinct mechanisms of loss generation have been identified, and their salient behaviors are described.

These mechanisms are as follows: (1) the mixing that occurs within the gap itself, caused by the separation bubble on the pressure surface edge; (2) mixing that occurs between the leakage jet and the mainstream flow, driven by a misalignment in flow direction; and (3) endwall loss at mid passage, where the flow is also unaligned with the relative motion of the endwall surface.

Some of these mechanisms are more prone to uncertainty than others. The separation bubble, subsequent mixing, and reattachment are well predicted, but these are often neglected from loss breakdowns, and the simplified isentropic tip model engineers use to interpret behaviors. Mixing with the mainstream is poorly predicted by RANS, and this is due to inadequate modeling of shear layers in most common turbulence models. The prediction of endwall shear in the 3D boundary layer suffers from two other issues, and the work input into the flow is too great and its rate of mixing with the rest of the flowfield is too slow.

3D design has shown new avenues of flowfield manipulation. Leaning the blade can reduce over tip mixing losses as the tip separation bubble size is reduced. Manipulating the camber distribution and lean in combination reduces misalignment between leakage jet and mainstream flow. Likewise, control over the location and the angle of the leakage jet aligns the flow better with the endwall motion. Experimental measurements show that balancing these three mechanisms allows reduction of losses in 30% of blade span by 18% relative to the datum design.

The challenge of the aerodynamicist is to minimize over acceleration of the flow, and this comes from the knowledge that high velocities will inevitably give rise to increased losses downstream. This article has shown that the loss mechanisms of tip leakage flows can be understood on the basis of the relative flow velocities. It is not necessary to resort to more esoteric interpretations of the fluid dynamics. Even for this nominally complex flowfield, aerodynamicists should simply strive to reduce their mismatches in velocity.

Acknowledgment

The authors would like to thank Rolls-Royce plc for their support and permission to publish this work, the EPSRC and UKTC for the computational time to run the DNS calculation on the UK's Archer and Archer 2 facilities, the ATI for their support during the iCore and Cordite research programmes, and TURBOSTREAM and 3DNS for the use of their flow solvers. They are also grateful for the comments and suggestions of colleagues at the Whittle Laboratory, Rolls-Royce, Siemens Energy, and Imperial College, most notably Rob Miller, Josh Maynard, Andrew Wheeler, John McGill, Tolga Yasa, Demetrios Lefas, Oliver Wadsworth, Chris Hall, John Bolger, Giuseppe Bruni, Senthil Krishnababu, Roger Wells, and Nicholas Cumpsty.

Conflict of Interest

There are no conflicts of interest.

Data Availability Statement

The authors attest that all data for this study are included in the paper.

Nomenclature

Roman and Greek Symbols

c = blade chord
d = tip clearance
r = radial direction
s = specific entropy
x = axial direction
A = area
P = pressure
U = surface velocity
V = fluid velocity
$\dot{m}$ = mass flowrate
α = yaw angle relative to axial direction
β = angle of leakage relative to blade camber
ϕ_v = viscous dissipation
θ = tangential direction
ρ = density
τ = shear stress

Subscripts

0 = stagnation condition
camber = parallel to camberline direction
in = inlet to stator row
leak = tip leakage direction
mix = difference between leakage and mainstream
normal = normal to camberline direction
out = outlet of stator row
peak = maximum value in gap
wall = rotating hub wall
PS = pressure surface
SS = suction surface

Nondimensional Groups

$P_{0,\mathrm{in}} - P_0/P_{0,\mathrm{in}} - P_{\mathrm{in}}$ = stagnation pressure loss coefficient
$P_{0,\mathrm{PS}} - P_{0,\mathrm{in}}/P_{0,\mathrm{in}} - P_{\mathrm{in}}$ = gap entry stagnation pressure coefficient
$P_{0,\mathrm{PS}} - P_{0,\mathrm{SS}}/P_{0,\mathrm{in}} - P_{\mathrm{in}}$ = gap loss coefficient
$T_{\mathrm{out}}(s_{\mathrm{in}} - s_{\mathrm{out}})/0.5{V_{\mathrm{in}}}^2$ = entropy loss coefficient
$\dot{m}_{\mathrm{normal}} dc/\dot{m}_{\mathrm{in}} A_{\mathrm{in}}$ = leakage flow/passage flow
$e^{s-s_{\mathrm{in}}/R}$ = entropy function
$\tau_\theta/0.5\rho {U_{\mathrm{wall}}}^2$ = endwall friction coefficient
$\phi_v c/\rho {V_{\mathrm{in}}}^3$ = dissipation coefficient

References

[1] Denton, J. D., 1993, "The 1993 IGTI Scholar Lecture: Loss Mechanisms in Turbomachines," ASME J. Turbomach., **115**(4), pp. 621–656.
[2] Rains, D. A., 1954, "Tip Clearance Flows in Axial Flow Compressors and Pumps," California Institute of Technology, Pasadena Mechanical Engineering Lab, Pasadena, CA, Technical Report.
[3] Storer, J. A., and Cumpsty, N. A., 1991, "Tip Leakage Flow in Axial Compressors," ASME J. Turbomach., **113**(2), pp. 252–259.

[4] Storer, J. A., and Cumpsty, N. A., 1994, "An Approximate Analysis and Prediction Method for Tip Clearance Loss in Axial Compressors," ASME J. Turbomach., **116**(4), pp. 648–656.

[5] You, D., Wang, M., Moin, P., and Mittal, R., 2007, "Large-Eddy Simulation Analysis of Mechanisms for Viscous Losses in a Turbomachinery Tip-Clearance Flow," J. Fluid. Mech., **586**, pp. 177–204.

[6] Tan, D., Li, Y., Chen, H., Wilkes, I., and Katz, J., 2015, "The Three Dimensional Flow Structure and Turbulence in the Tip Region of an Axial Flow Compressor," Volume 2A: Turbomachinery of Turbo Expo: Power for Land, Sea, and Air, Montreal, Quebec, Canada, June 15–19.

[7] Seki, R., Azuma, T., Iwatani, J., Nakaniwa, A., Okui, H., and Shibata, T., 2023, "Investigation of Tip Leakage Vortex Breakdown in a High-Speed Multistage Axial Compressor," ASME J. Turbomach, **145**(7), p. 071017.

[8] Maynard, J. M., Taylor, J. V., Wheeler, A. P. S., and Wells, R., 2023, "Unsteady Structure of Compressor Tip Leakage Flows," ASME J. Turbomach., **145**(5), p. 051005.

[9] Dawes, W. N., 1987, "A Numerical Analysis of the Three-Dimensional Viscous Flow in a Transonic Compressor Rotor and Comparison With Experiment," ASME J. Turbomach., **109**(1), pp. 83–90.

[10] Ventosa-Molina, J., Lange, M., Mailach, R., and Fröhlich, J., 2020, "Study of Relative EndWall Motion Effects in a Compressor Cascade Through Direct Numerical Simulations," ASME J. Turbomach., **143**(1), p. 011005.

[11] Bruni, G., Taylor, J., Krishnababu, S., Miller, R., and Wells, R., 2020, "Squealer Tip Treatment Design for Axial Compressors," Turbo Expo: Power for Land, Sea, and Air, Vol. 84065, Online, September, American Society of Mechanical Engineers, p. V02AT32A035.

[12] Taylor, J. V., 2015, "Three-Dimensional Mechanisms in Compressor Flows," Ph.D. thesis, Department of Engineering, University of Cambridge, Cambridge, UK.

[13] Taylor, J. V., 2019, "Complete Flow Conditioning Gauzes," Experiments Fluids, **60**(3), pp. 1–7.

[14] Taylor, J. V., and Miller, R. J., 2016, "Competing Three-Dimensional Mechanisms in Compressor Flows," ASME J. Turbomach., **139**(2), p. 021009.

[15] Taylor, J., Conduit, B., Dickens, A., Hall, C., Hillel, M., and Miller, R., 2020, "Predicting the Operability of Damaged Compressors Using Machine Learning," ASME J. Turbomach., **142**(5), p. 051010.

[16] Dickens, T., Taylor, J., Hall, C., and Miller, R., 2021, "Aerodynamic Mitigation of Mechanical Constraints in Small Compressor Blade Profiles," Volume 2A: Turbomachinery—Axial Flow Fan and Compressor Aerodynamics of Turbo Expo: Power for Land, Sea, and Air, Online, June, p. V02AT31A032.

[17] Tam, C. K., and Webb, J. C., 1993, "Dispersion-Relation-Preserving Finite Difference Schemes for Computational Acoustics," J. Comput. Phys., **107**(2), pp. 262–281.

[18] Wheeler, A. P. S., Dickens, A. M. J., and Miller, R. J., 2018, "The Effect of Nonequilibrium Boundary Layers on Compressor Performance," ASME J. Turbomach., **140**(10), p. 101003.

[19] Przytarski, P. J., and Wheeler, A. P. S., 2021, "Accurate Prediction of Loss Using High Fidelity Methods," ASME J. Turbomach., **143**(3), p. 031008.

[20] Przytarski, P. J., and Wheeler, A. P., 2021, "Accurate Prediction of Loss Using High Fidelity Methods," ASME J. Turbomach, **143**(3), p. 031008.

[21] Brandvik, T., and Pullan, G., 2010, "An Accelerated 3D Navier Stokes Solver for Flows in Turbomachines," ASME J. Turbomach., **133**(2), p. 021025.

[22] Spalart, P., and Allmaras, S., 1992, "A One Equation Turbulence Model for Aerodynamic Flows," AIAA. J., **94**, p. 439.

[23] Drela, M., and Youngren, H., 1998, "A User's Guide to MISES 2.53," Massachusetts Institute of Technology, Cambridge, MA.

[24] Khalid, S. A., Khalsa, A. S., Waitz, I. A., Tan, C. S., Greitzer, E. M., Cumpsty, N. A., Adamczyk, J. J., and Marble, F. E., 1999, "Endwall Blockage in Axial Compressors," ASME J. Turbomach., **121**(3), pp. 499–509.

[25] Schlichting, H., and Gersten, K., 1999, *Boundary Layer Theory*, Springer, New York.

[26] Gallimore, S. J., and Cumpsty, N. A., 1986, "Spanwise Mixing in Multistage Axial Flow Compressors: Part I—Experimental Investigation," ASME J. Turbomach., **108**(1), pp. 2–9.